

國立台灣大學理學院應用物理研究所

碩士論文

Graduate Institute of Applied Physics

College of Science

National Taiwan University

Master Thesis

結合超寬頻光源以提供光譜解析度的

共軛焦雷射掃描眼底鏡

Spectrally Resolved Confocal Scanning Laser
Ophthalmoscopy Based on Supercontinuum

The seal of National Taiwan University is a circular emblem. It features a central design with a scale of justice and a book, surrounded by the university's name in Chinese characters: '國立台灣大學' at the top and '愛·學勵' at the bottom.

鄭岳弘

Yueh-Hung Cheng

指導教授：朱士維 博士

Advisor: Shi-Wei Chu, Ph.D.

中華民國 99 年 7 月

July, 2010

誌謝

感覺就好像加入了一個夏令營一樣，兩年的時間說長不長說短不短，一下就過了。回想當初大四準備研究所的過程，就覺得能到台大讀書真的是出乎預料。當初對於讀研究所的動機，主要是為了就業需要的學歷做準備，不過其實心裡也很想把四大力學好好的再重溫一次。

不過計畫跟不上變化，經過一番折騰，我來到了這間以生物及光學為主軸的實驗室。記得當初高二分組的時候，我是鐵了心不要讀生物的，大學的光學課也是休得上不下。在這個時候，給我最多幫助的就是我的指導教授朱士維。謝謝教授給我們很大的空間自己摸索，並且也認真跟我們討論遇到的問題。在我參加研討會及撰寫論文拖拖拉拉的時候，也能夠耐心的給我指導。謝謝口試委員孫啟光教授及王致恬教授擔任我的口試委員。雖然當時口試準備得很匆忙，但是你們仍然給了我許多很寶貴的意見。謝謝蔡懷禎教授提供我實驗用的斑馬魚。謝謝媽媽對我忙碌的實驗室生活的體諒，並且讓我在從新竹回來後重新體會到住在家裡的好。謝謝鈞彥在我大一的時候給我的幫助。每當坐在實驗室想到什麼的時候，抬起頭來就可以跟鈞彥討論。無論在做事及做人方面，都是我的模範。能夠遇到這樣的學長，真的是我的好運。謝謝宗衍跟建盛，陪伴了我許多個比罰球的午後，那段時間我飲料喝了很多。謝謝翰軒讓我在電路跟程式有那麼一點點的小進步。謝謝柏峻能夠接手這個系統。謝謝所有學長學弟們陪伴我度過許多實驗室的時光，也謝謝大家容忍我暴躁的脾氣。特別要謝謝舒怡，在我情緒失控或是忙碌的時候都能夠陪伴我，有妳陪伴對我真的很重要。

無論這兩年我有甚麼的進步，都不是因著我自己。因為有你們，我才能完成這個學位。無論將來有甚麼不起眼的成就，也都是你們的功勞。

摘要

視網膜是一個由掌管視覺影像的神經所組成之脆弱的層狀組織。現代科學家藉由非侵入式顯微術如共軛焦雷射掃描眼底鏡，即可得到視網膜的資訊，同時藉由此唯一的窗口進行不傷害身體的血管健康觀測。共軛焦雷射掃描眼底鏡能提供視網膜的三維結構，對於視網膜病變的診斷有很大的用處。由於疾病往往伴隨化學成分的改變，具光譜解析度的雷射掃描眼底鏡可以藉由樣品的光譜變化而早期發現疾病。此外因為視網膜上的神經細胞對於光線的波長極為敏感，具光譜解析度的眼底鏡能藉由不同波長的光激發視神經，讓神經科學有更大的想像空間。

過去曾經有人嘗試將光譜影像能力與雷射掃描眼底鏡結合以在活體中進行視覺的色彩研究。然而這些研究都受到了雷射光源以及系統的像差影響。我們提出一套結合超寬頻光源的雷射掃描眼底鏡。藉由光子晶體光纖內的非線性效應，我們可以將單一波長的紅外光雷射換成頻寬由可見光到紅外光的光源。此外我們也以面鏡架設了一套具有繞射極限性能的雷射掃描眼底鏡，以克服一般透鏡系統的色像差。這套系統讓我們能以非侵入式的方法取得活體視網膜的光譜影像，同時簡化以往同類型實驗的步驟。另外這樣的系統也讓我們可以自由選擇光的波長以用來激發視神經，並且觀察神經的訊號傳遞。

Abstract

Retina is a fragile layered tissue composed of neurons responsible for color vision. It is not only part of central nervous system (CNS) which can be investigate noninvasively, but also the only window that microscopic inspection of circulation system can be taken without invasion. A confocal scanning laser ophthalmoscope (cSLO) provides three-dimensional structure of retina, which is important to retinopathy diagnosis. As diseases usually occur with biomedical change of tissue, a spectrally resolved cSLO can diagnose the illness in the early stages by analyzing absorption spectrum of the tissue. Furthermore, because the neurons on retina are sensitive to the wavelength of the light exposed to, a spectrally resolved cSLO facilitates the studies of the neuroscience about retina.

There have been several attempts of spectrally resolved cSLO, but the performances of those systems were all limited by the bandwidth of the lasers and the chromatic/geometric aberration of optics. Here a spectrally resolved cSLO with bandwidth from visible to infrared is demonstrated. The broadband light source is a supercontinuum laser, which is generated from the nonlinear effects in a photonic crystal fiber. We also construct a mirror-based scanning system with diffraction-limited performance, overcoming the aberration problems in previous multispectral systems. With this system, spectral images of living retina from visible to infrared are acquired in a noninvasive manner. Resolution is around $3\mu\text{m}$ in living zebrafish, which is adequate for cone cell recognition and researches about retina, vision and neuroscience.

目 錄

口試委員會審定書	1
誌謝	2
中文摘要	3
英文摘要	4
第一章視網膜光譜影像的重要性	
第一節 視網膜影像之應用	9
第二節 具光譜解析度之視網膜影像之可能性	11
第二章 視網膜光譜影像技術比較	
第一節 眼底攝影機	14
第二節 共軛焦雷射掃描眼底鏡	18
第三節 視網膜光學同調斷層掃描	25
第四節 技術比較及結論	27
第三章 系統架設	
第一節 概論	31
第二節 光源	32
第三節 掃描系統	34
第四節 訊號偵測及影像擷取	36

第五節 零件規格	37
第四章 結果及討論	
第一節 以人工眼模擬視網膜光譜影像	40
第二節 斑馬魚的視網膜眼底影像	43
第三節 結論	52
圖目錄	53
表目錄	54
參考文獻	55



Contents

Thesis committee approval	1
Acknowledgement	2
Chinese abstract	3
English abstract	4
Chapter I Importance of retinal spectral imaging	
I.1 Retinal imaging and applications	9
I.2 Potential of retinal spectral imaging	11
Chapter II Comparison between retinal imaging techniques	
II.1 Fundus camera	14
II.2 Confocal scanning laser ophthalmoscopy (cSLO)	18
II.3 Optical coherence tomography (OCT)	25
II.4 Discussion and conclusion	27
Chapter III Experimental setup	
III.1 Overview	31
III.2 Light source	32
III.3 Scanning system	34
III.4 Signal detection and image acquisition	36

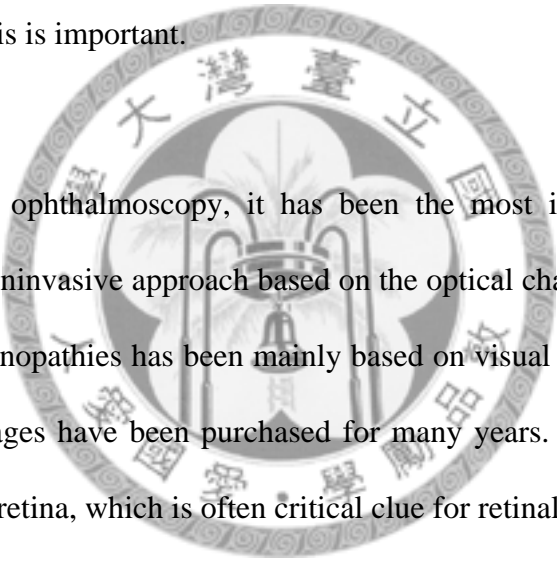
III.5	Specification of devices	37
Chapter IV Result and discussion		
IV.1	Spectral images of artificial eye	40
IV.2	Retinal spectral images of zebrafish	43
IV.3	Conclusion	52
Figure index		53
Table index		54
Reference		55



Chapter I Importance of Retinal Spectral Imaging

I.1 Retinal Imaging and Applications

Retina is part of the central nervous system (CNS) and responsible of visual signal perception. It is like the film for a camera but possesses much more complex functions and mysteries. The dependence on vision in every single day tells the importance of a healthy retina. Retinal pathologies have been the troubles for ophthalmologists because the damages on retina are usually irreversible and may harm one's vision. The fragility of retina makes invasive surgery on human eye not reasonable in most case, so a tool for early retinal disorder diagnosis is important.



After the invention of ophthalmoscopy, it has been the most important apparatus for ophthalmology. This noninvasive approach based on the optical characteristic is perfect for retina. Diagnosis of retinopathies has been mainly based on visual impression. As a result, high quality retinal images have been purchased for many years. Retinal images provide detailed information of retina, which is often critical clue for retinal pathologies.

For example, glaucoma causes structural changes to optic nerve head and nerve fiber layer[1]. Stereoscopic images of optic nerve head provide thickness, area and other parameters. This information is important to early detection of glaucoma, which prevents visual loss and simplifies treatments.

On the other hand, retinopathy is also found to be the most common microvascular complications of diabetes, which include microaneurysm formation and oxidative

damage[2]. Screening of these retinopathies is of significance and feasible with a fluorescent retinal imaging. By tracking the fluorescent dye, formation of microaneurysm and vascular damage are found with higher contrast.

Another example is age-related macular degeneration (AMD), which is the leading cause of blindness in the developed world. Drusen and extracellular material accumulating in the inner aspects of Bruch's membrane appears with AMD. Generally, larger drusen are associated with changes in fundus autofluorescence[3].

Besides the applications for retinopathy diagnosis, retinal imaging also benefits biomedical research for its ability to *in-vivo* observation of cell movement in retina and choroidal blood vessel like measurement of the level of leukocyte recruitment[4], which is an indicator of inflammation. However, studies of leukocyte and its behavior usually require *ex vivo* tissue from vessel of living animal exteriorized by surgery. This method is not practical for fragile subject like retina or other parts of the central nervous system. With retinal images, *in-vivo* observation of leukocyte without altering physiological situation in body is feasible without surgery.

A different way to exploit the possibility of retinal imaging system is to stimulate the photoreceptors on retina. By illuminating a part of retina, degree of scotoma can be identified, which often appears with retinopathies. Optical stimuli on retina also enable studies of vision process in central nervous system. By stimulating the photoreceptors on retina, visual evoked responses can be recorded with electrodes[5]. Understanding the relation between stimuli and responses helps realize the formation of vision.

In summary, retinal imaging is useful for retinopathy diagnosis and biomedical research. By acquiring *in-vivo* information, ophthalmologists and biologists can obtain information with minimal invasion without changing local physiological situation.

I.2 Potential of Retinal Spectrally Imaging

At the early stage of development of ophthalmoscope, flame, daylight and bulb are used as illumination source. These illumination sources possess broad spectrum and produce “white light” images, in which information of all wavelengths overlaps in a single frame. However, monochromatic retinal images produced with band pass filters are later found to provide better contrast of various structures. Since then, retinal imaging systems with illumination sources of different wavelengths have been used in applications like structure identification, retinopathy diagnosis, microcirculation monitoring and neuroscience researches.

As retina is part of the central nervous system and is related to color vision, it is not surprising that the reflectance of retina is related to the chemical concentration of local tissue. Retinal spectral images can be used to identify the structures with their spectral characteristic. For example, illumination from 460 to 560 nm enhances the contrast of the nerve fiber layer compared with other wavelengths. Macular pigment absorbs light between 390 and 540 nm, acting as a blue light filter[6]. Reflectances of three types of cone cells, which are responsible of color vision, exhibit different spectral characteristics. Identifying spectral information of tissue helps ophthalmologists assess the condition of retina faster and more accurately. On the other hand, reflectance of pigments from spectral retinal image provides valuable data for ophthalmic research.

Besides composition of retina, deformation and denaturation caused by retinopathy also affect spectral feature of retina. Thus multicolor images supply more clues than a monochromatic image for diagnosis of retinopathy. For example, glaucoma alters the extinction of fundus pigments like oxyhemoglobin, xanthophyll and rhodopsin. Changes of local reflectance in the papilla-macular bundle and nerve fiber layer are results of decreases of these pigments and is thought as symptoms of glaucoma at the early stage[7]. As for diabetes, alternation in the fundus happens in the early stage and induces changes in reflectance spectrum. In the red side of visible range, reflectance shows significant difference between normal macular and macular with diabetic retinopathy. The contrast comes from the reduction of melanin pigment due to diabetes[8].

There are some hereditary ophthalmic diseases that show spectral characteristics, too. Retinitis pigmentosa is one of those inherent diseases. It may be transmitted on the X-chromosome and carrier of this type of retinitis pigmentosa shows special reflex in the perimacular region, which is named tapetal-like reflex (TLR). It causes cone dystrophy and dysfunction. TLR presents higher reflectance than normal subject from 600 nm to 400 nm and thus can be observed with retinal spectral images[9].

Since there is a difference between absorption characteristics of oxygenated and deoxygenated blood, retinal spectral imaging is also used to monitor oxygen saturation, which is linked to microcirculation[10]. Understanding the microcirculation *in-vivo* is crucial for investigating the role of oxygenation in nature healing and clinical therapies. Methods like oxygen microelectrodes, magnetic resonance imaging have been proposed. However, these methods are either invasive or with poor spatial resolution. Optical

imaging of retina provides necessary information with minimal invasiveness and cellular resolution, which is the best way for related studies.

Except clinical applications, spectral stimuli are also helpful to spectral researches about the visual signal perception and transduction. For example, photoreceptors of different types are sensitive to different wavelength range of illumination. The triggering of signals corresponding to different colors and their following neural activities are important to understanding the central nervous system. In a previous study, blue light illuminated the entire retina and the intensity was modulated to identify the blue-yellow color opponent pathway of rod and cone photoreceptors. The intensity level of illumination determines the origin of signal, since rods have not only higher sensitivity but also lower saturation intensity than cones. By recording the signal under different illumination intensity, pathway of rods and cones can be distinguished[11].

In conclusion, retinal spectral images can not only accomplish the applications of the traditional with monochromatic light source, but also provide contrast comes from illumination of different wavelengths. The flexibility of wavelength in point illumination on retina provides enhanced contrast by providing spectral information for the uses of structure identification and retinopathy diagnosis. Neuroscience researches are also benefited by spectrally resolved stimuli because of the possibility of wavelength-dependent neuron excitation.

Chapter II Comparison between Retinal Imaging Techniques

In the last chapter, we talked about the potentials of retinal spectral imaging. Each of the applications has specific requirements. There are several retinal imaging techniques that are able to carry out retinal spectral imaging. They are fundus camera, confocal scanning laser ophthalmoscopy and optical coherence tomography. The difference in principles between these imaging manners results in their particular applications. In this section, comparisons of resolution, three-dimensional imaging capability, frame rate, spectral imaging adaptability and other characteristics between these three methods will be discussed.

II.1 Fundus Camera

The most common instrument for an ophthalmologist is an ophthalmoscope. After the first ophthalmoscope invented by Helmholtz in 1850, ophthalmologists have been able to investigate retina without invasion, which is important to clinics. However, image quality may be affected by skill of ophthalmologists and it is also difficult to make quantitative analysis. Those problems are solved by introducing a CCD into an ophthalmoscope for signal detection. This kind of system is called fundus camera. It is just an optical microscope, except that the objective is replaced by the ocular lens.

Although the imaging quality of fundus camera is worse than optical microscopy because of the aberration of the eye, we still treat it as a diffraction-limited system in the following paragraphs for convenience. From now on we deal the eye as a simplified model which is composed of an aberration-free lens and a piece of retina.

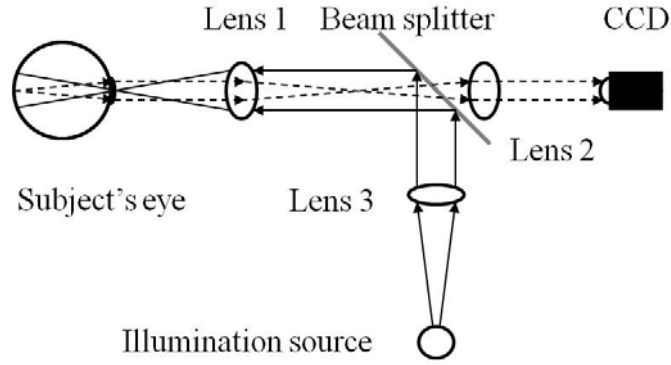


Fig. 2.1 Setup of a fundus camera. Dashed: signal from subject.

The resolution of an ideal fundus camera is limited by the geometry of the subject's eye. To calculate the transverse resolution of an eye, let us assume a lens at YZ plane, centered at (0, 0, 0) with diameter \mathbf{D} and focal length \mathbf{f} . The electric field at the lens is in phase and propagate along X direction. The electric field at a point $\mathbf{R} = (\mathbf{X}, \mathbf{Y}, \mathbf{Z})$ contributed by an infinite area $d\mathbf{S}$ at $(\mathbf{0}, \mathbf{y}, \mathbf{z})$ on the lens is

$$d\mathbf{E} = \frac{\varepsilon_0}{\mathbf{R}} e^{i(\omega t - kr)} d\mathbf{S}$$

, where ε_0 is the amplitude of electric field and r is

$$r = [\mathbf{X}^2 + (\mathbf{Y} - \mathbf{y})^2 + (\mathbf{Z} - \mathbf{z})^2]^{\frac{1}{2}} = \mathbf{R} \left[1 + \frac{(\mathbf{y}^2 + \mathbf{z}^2)^2}{\mathbf{R}^2} - 2 \frac{(\mathbf{Yy} + \mathbf{Zz})}{\mathbf{R}^2} \right]^{\frac{1}{2}}$$

, which is the displacement between $d\mathbf{S}$ and \mathbf{P} . Under Fraunhofer condition, which means

\mathbf{R} is much larger than the dimension of the aperture, r can be approximate as

$$r \cong \mathbf{R} \left[1 - 2 \frac{(\mathbf{Yy} + \mathbf{Zz})}{\mathbf{R}^2} \right]^{\frac{1}{2}} \cong \mathbf{R} \left[1 - \frac{(\mathbf{Yy} + \mathbf{Zz})}{\mathbf{R}^2} \right]$$

For the circular aperture of eye, it suggests introducing spherical coordinates. Thus

$$\mathbf{z} = \rho \cos \phi \quad \mathbf{y} = \rho \sin \phi$$

$$\mathbf{Z} = \eta \cos \varphi \quad \mathbf{Y} = \eta \sin \varphi$$

By integrating over the entire lens, we obtain the electric field \mathbf{E} at \mathbf{P}

$$\begin{aligned}\mathbf{E} &= \iint_{\text{Aperture}} d\mathbf{E} = \iint_{\text{Aperture}} \frac{\varepsilon_0}{\mathbf{R}} e^{i(\omega t - kr)} d\mathbf{S} \\ &= \frac{\varepsilon_0}{\mathbf{R}} e^{i(\omega t - k\mathbf{R})} \int_0^{\frac{D}{2}} \int_0^{2\pi} e^{i\left(\frac{k\rho\eta}{\mathbf{R}}\right) \cos(\Phi - \varphi)} \rho d\rho d\Phi\end{aligned}$$

We can see that the resulting electric field is Fourier transform of the aperture field.

Because of the axial symmetry of the solution, we choose $\varphi = \mathbf{0}$ for simplification. Here

we introduce the Bessel function of order zero

$$J_0(u) = \frac{1}{2\pi} \int_0^{2\pi} e^{iu \cos v} dv$$

By replacing the angular integral with Bessel function, we have

$$\mathbf{E} = \frac{\varepsilon_0}{\mathbf{R}} e^{i(\omega t - k\mathbf{R})} * 2\pi \int_0^{\frac{D}{2}} J_0\left(\frac{k\rho\eta}{\mathbf{R}}\right) \rho d\rho$$

With a property of the Bessel function,

$$\frac{d}{du} [u^m J_0(u)] = u^m J_{m-1}(u)$$

We have

$$\mathbf{E} = \frac{\varepsilon_0}{\mathbf{R}} e^{i(\omega t - k\mathbf{R})} * 2\pi \left(\frac{D}{2}\right)^2 \left(\frac{2\mathbf{R}}{kD\eta}\right) J_1\left(\frac{kD\eta}{2\mathbf{R}}\right)$$

So the intensity pattern, which is also called the point-spread function, is

$$\mathbf{P} = \frac{2\varepsilon_0^2 A^2}{\mathbf{R}^2} \left[\frac{J_1\left(\frac{kD\eta}{2\mathbf{R}}\right)}{\frac{kD\eta}{2\mathbf{R}}} \right]^2 = \mathbf{I}(0) \left[\frac{2J_1\left(\frac{kD}{2} \sin \theta\right)}{\frac{kD}{2} \sin \theta} \right]^2$$

, where $\mathbf{I}(0) = \frac{\varepsilon_0^2 A^2}{2\mathbf{R}^2}$ and $\sin \theta = \frac{\eta}{\mathbf{R}}$.

The lateral resolution is defined by the first dark fringe of the intensity pattern

$$\eta = 1.22 \frac{\mathbf{R}\lambda}{D} = 1.22 \frac{\mathbf{R}\lambda_0}{nD} \cong 0.61 \frac{\lambda_0}{NA}$$

, where $\lambda_0 = n\lambda$ is the wavelength in air. NA is the abbreviation of numerical aperture, which is defined as

$$NA = n \sin \theta$$

, where θ is the half angle of the cone of light converging to the illuminated spot. For a fundus camera, wavelength and NA are two important parameters to define resolution. Typically, NA in human eye increases from 0.1~0.3 with increasing light level.

We can find the longitudinal resolution by similar method. The on-axis intensity at \mathbf{X} away

from focus is proportional to $\left(\frac{\sin \frac{\xi}{4}}{\frac{\xi}{4}}\right)^2$, where

$$\xi = \mathbf{X} \frac{2\pi}{\lambda n} NA^2$$

So we can find the first axial intensity minimum from focus at

$$\mathbf{X} \frac{2\pi}{\lambda n} NA^2 = \pm\pi$$

, which determines the longitudinal resolution. With the equations above, we are able to calculate the diffraction-limited resolution of eyes. For example, with an eye whose NA is 0.1 and 630 nm illumination, the lateral and axial resolution is 3.8 μm and 44.2 nm respectively.

Frame rate is a big issue because even if the subject tries to keep eye fixed, saccade may still happen without control. The frequency of saccade is around 10 Hz[12]. To overcome the saccade and the consequential blur, frame rate is usually designed as video rate so that images can be taken between saccades. Because of the scanless imaging principle of fundus camera, its frame rate is restricted by the acquisition rate of CCD, which is normally several tens or hundreds of frame per second.

By combining appropriate arc lamps and filters, fundus camera can acquire retinal spectral images. The spectral resolution of a fundus camera is only restricted to the bandpass region of the filter, which can be 10 nm or lower.

As fundus camera receive scattered light from retina, reflected light from cornea and anterior surface of the crystalline lens are also detected, downgrading contrast of images. To avoid these reflections, illumination of fundus camera is usually in a shape of a ring. This way, illumination and signal pass through separated path. Usually pupil is dilated so that larger aperture can be attained.

II.2 Confocal Scanning Laser Ophthalmoscopy

Another important ophthalmic tool was published in 1980s. At that moment, confocal microscope boomed with the development of laser and other photonic technologies. Webb et al. built the first confocal scanning laser ophthalmoscope(cSLO)[13] based on the concept of reflection confocal scanning laser microscope(CSLM)[14,15]. Fig. 2.2 is a diagram of confocal microscopy. A point light source is imaged at the subject and the scattered light is collect by the lens. A pinhole is introduced to block the out-of-focus light form the subject and it enables a confocal microscope to collect signal from a single layer. This is called optical sectioning, which is an important milestone of optical imaging. Confocal integrated optical imaging techniques are widely applied because of it ability to imaging area under the surface of subjects through optical sectioning.

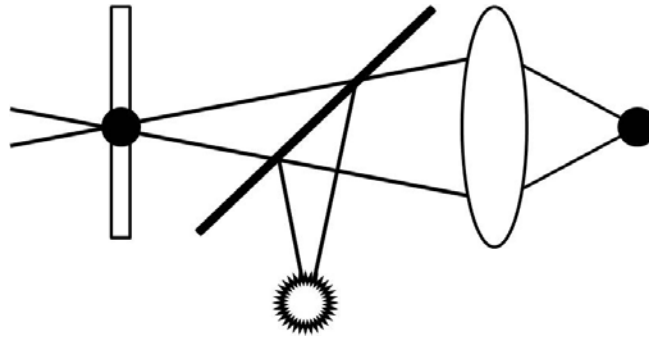


Fig. 2.2 Concept of confocal microscope. Light from a point light source illuminates a single point. The pinhole blocks most of the scattered light except from the focal point.

To find the resolution of cSLO, we also need to calculate the point-spread function. There is some difference between cases of cSLO and fundus camera. First, cSLO uses laser as light source, which means the aperture is not illuminated uniformly. Second, the confocal pinhole changes the effective point-spread function of cSLO.

The point-spread function of a focused laser beam is calculated by Gaussian beam analysis. The equation of Gaussian beam is

$$E = \frac{1}{q} e^{ikq} e^{-ik\left(\frac{\rho^2}{2q}\right)}$$

, in which q is the complex radius of curvature, k is the wave number and ρ is the radius from optical axis. As we know that the focused electric field is the Fourier transform of the Gaussian beam, which is also Gaussian beam, the lateral resolution can be defined by its beam spot size ω . Suppose the beam propagates along Z axis. The transformation of the complex radius of curvature and the beam spot size of a Gaussian beam

$$\frac{1}{q} = \frac{1}{z - iz_0} = \frac{1}{R} + i \frac{\lambda}{\pi\omega^2 n}$$

follows the ABCD matrix of ray optics, where R is the radius of curvature of wavefront, n

is the refractive index and λ is the illuminating wavelength. The radius of curvature R is defined as

$$R = z \left(1 + \frac{z_0^2}{z^2} \right)$$

The ABCD matrix gives

$$q' = \frac{Aq + B}{Cq + D}$$

Now we suppose a Gaussian beam is focused by a thin lens. We further assume that the beam is collimated at the lens. Thus at both lens and the focus R is approaching infinity.

Now we have

$$q_1 = -iz_1 = -i \frac{\pi \omega_{01}^2 n}{\lambda} \quad \text{and} \quad q_2 = -iz_2 = -i \frac{\pi \omega_{02}^2 n}{\lambda}$$

The matrix elements give the transformation equations of q ,

$$\begin{cases} ACz_1^2 + BD = 0 \\ z_2 = \frac{z_1}{Cz_1^2 + D} \end{cases}$$

Here we introduce the ABCD matrix of a thin lens with focal length f , which is

$$\begin{bmatrix} 1 - \frac{d}{f} & d \\ -\frac{1}{f} & 1 \end{bmatrix}$$

So the transformation equations become

$$\begin{cases} \left(1 - \frac{d}{f} \right) \left(-\frac{1}{f} \right) z_1^2 + d = 0 \\ z_2 = \frac{z_1}{\frac{1}{f^2} z_1^2 + 1} \end{cases}$$

Typically, $z_1 \gg f$. By solving the equations with this approximation, we have

$$\begin{cases} d = f \\ \omega_{02} = \frac{\lambda}{\omega_{01} \pi n} f \end{cases}$$

The beam spot size ω_{02} at focus determines the transverse resolution of wide-field

microscopy.

However, because only a portion of scattered light will pass the confocal pinhole, we need to find the effective point spread function of entire system. The point-spread function \mathbf{P} of the pinhole represents the observed volume by the detector, so the effective confocal point spread function \mathbf{P}_{conf} is simply the product of \mathbf{P} of illumination and observation. Suppose the diameter of the pinhole approaches zero, then the point-spread function of the pinhole is identical to the illumination one because identical optics are shared. Thus we have

$$\mathbf{P}_{\text{conf}} = \mathbf{P}^2 \propto e^{-\left(\frac{2\rho}{\omega_{02}}\right)^2}$$

In this equation we can see the beam spot size is reduced by a factor of $\sqrt{2}$, enhancing lateral resolution. The axial resolution is defined by the confocal parameter $2z_2 = 2\frac{\pi\omega_{02}^2 n}{\lambda}$, within which the beam spot size hasn't diverged to be larger than $\sqrt{2}\omega_{02}$.

Discussion above is for an underfilled aperture. However, objectives are usually overfilled to not spoil the resolution too much. The resulting point-spread function would be a mixed diffraction pattern of Gaussian and plane wave. If we cut the Gaussian beam at ω , only 14% of light is lost and the resolution is spoiled very little from plane wave case[15].

A cSLO is composed of four main components, including laser source, scanning system, signal detection and frame grabbing. Light from a laser source is first sent into a scanning system, which is used to change the illuminated point on the subject. There are many scanning strategies for CSLM like stage scanning, moving pinhole scanning and moving laser-beam scanning, but only some of them are suitable for cSLO. In the following paragraphs I am going to discuss the compatibility between cSLO and the scanning

strategies.

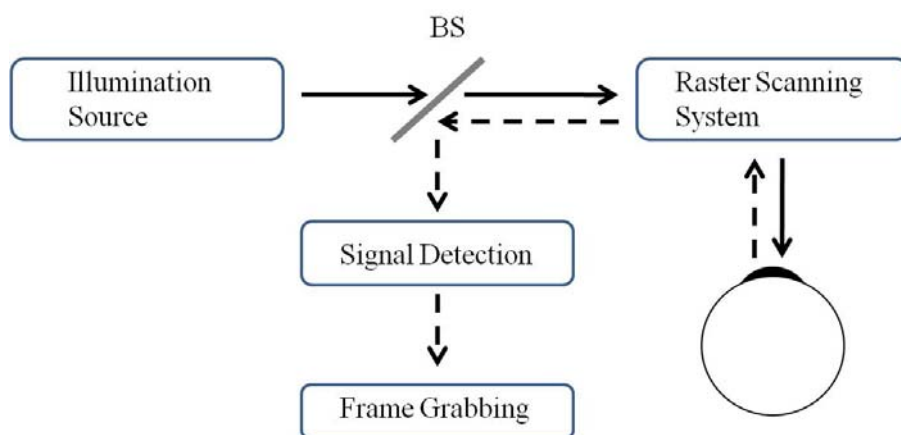


Fig. 2.3 The scheme of a cSLO. BS: Beam splitter. Solid: Illumination. Dashed: signal.

Stage scanning is achieved by changing the position of sample, usually by a translational stage, to illuminate different spots on subject. The advantages of stage scanning are wide field of view regardless of optics and the optics work on axis, which makes diffraction limited performance achieved easier. It is the simplest scanning strategy but not suitable to retinal imaging. The frame rate of stage scanning, which is usually several seconds per frame, is too low to overcome the eye saccade.

Moving pinhole scanning is achieved by changing the position of source and detection point in the image plane. By increasing the number of pinhole, signal from multiple points is collected at the same time, thus increasing the frame rate. Common setup includes a pair disk on which are a pinhole array and a microlens array. By rotating the disk we are able to observe different points at subject. For a typical disk with 200,000 pinholes rotating at 2,000 rpm, it is possible to achieve 700 frame/sec. The problem of this strategy is the loss

of the illumination energy. To fill every lens in the microlens array at the same time, light source must overfill the array. This causes great energy loss of illumination. Although this may be overcome by introducing high power lamp, absorbed light overheats the disk and downgrades the performance. The difficulty of manufacture of pinhole and microlens array also increases the cost of system.

Typically, moving laser-beam scanning is achieved by a pair of scanning mirrors, which are used to change the direction of beam in two orthogonal axes. However it is impossible to guide the beam into pupil with simply two scanning mirrors. A telescope or two are required to relay the optical path onto pupil. The frame rate of moving laser-beam scanning system is determined by the frequency of the scanning mirrors. To achieve video rate scanning to overcome the saccade, spinning polygonal mirror and resonant scanner are common choices of scanner.

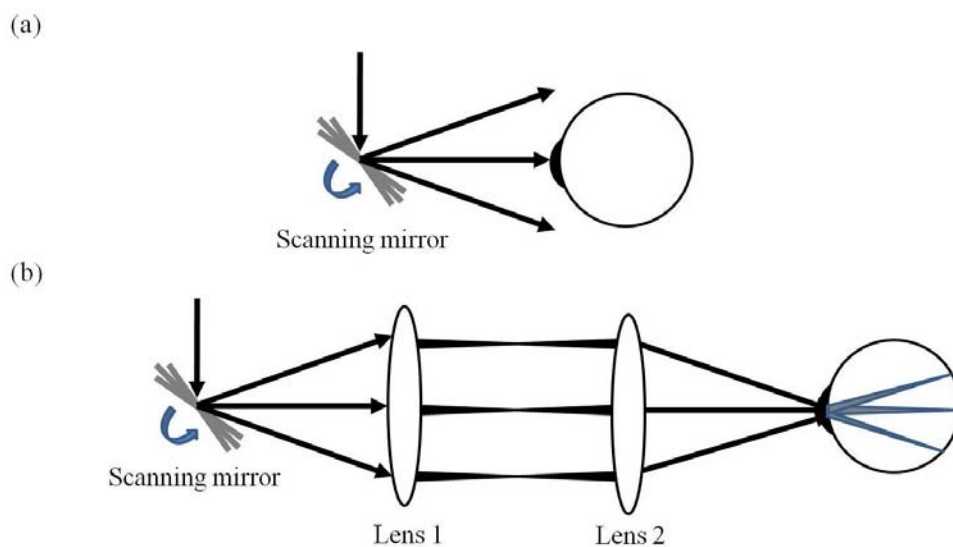


Fig. 2.4 Telescope for moving beam scan. (a) Without relaying optics, the scanning laser beam is not able to enter pupil. (b) A telescope is used to relay the scanning beam onto pupil.

Polygonal mirror is popular for its unidirectional scans, large apertures, and large scanning angles. Its high angular velocity and multiple facets provide scanning frequency at several tens of kHz, which is adequate for video rate scanning. The drawbacks of it are the moving instantaneous center-of-scan and the quality difference between the facets. The movement of instantaneous center-of-scan is because the axis of rotation does not fall on the reflecting surface. This would give rise to the conjugate point movement at the back aperture of the objective and the corresponding aberration.

As for resonant scanner, which is known for its simplicity and small size, it has been widely used to video rate scanning systems. Unlike in the case of polygonal mirror, the rotation axis coincides with the reflecting surface, giving stationary conjugate point. The disadvantage of resonant scanner is its sinusoidal motion and dual-directional scans. The sinusoidal motion distorts the image because of the inconsistency of angular velocity during scans and the dual-directional scans waste half of the scanning time.

The scanning laser beam is focused onto retina by the ocular lens after passing through the scanning system. The scattered signal from retina goes back through the same path and separated from the incident beam by a beam splitter. Finally, the light signal is transformed into electronic signal by a photodetector. Photomultiplier tube (PMT) is the most commonly used detector. PMT is based on the photoelectric effect. In PMT, photons first strike the photocathode and then photocathode emits photoelectrons. The emitted photoelectrons would enter an electron multiplier and experience secondary amplification. The resulting amplified current signal is then received by a frame grabber. With proper algorithm, the signal will be divided in to sequence with respect to time and arranged into a picture point by point.

II.3 Optical Coherence Tomography

Optical coherence tomography (OCT) is a imaging technique published in 1991[16]. The principle of OCT is similar to ultrasound imaging, except the sound wave is replaced by electromagnetic wave. The shorter wavelength of light results in lower penetration depth than ultrasound, while resolution is improved by around two orders of magnitudes.

The principle of OCT is based on interference. In an OCT, a light source is separated into sample field E_s and reference field E_r . The two fields are recombined after reflected and interfere with each other. The intensity at the detector is

$$I_d = 0.5 \times (E_r + E'_s)^2 = 0.5(I_r + I'_s) + \text{Re}(E_r^*(t + \tau)E'_s(t))$$

, where E'_s is the sample field scattered back from the sample and τ is the optical time delay controlled by the length of the reference arm. The second term is related to τ and the characteristic of sample. By controlling τ , E'_s is calculated from the interference intensity measured at the detector with proper algorithm. By moving the reference mirror, OCT collects depth information of single point, which is called A-scan.

Because only when optical path difference between is shorter than coherence length there will be interference, coherence length is directly related to axial resolution of OCT. With low-coherence laser, axial resolution of OCT can be shorter than $1\mu\text{m}$ [17], while lateral resolution is restricted by the numerical aperture. Retinal researches of OCT began right after the publication in 1991, and it has been an important diagnostic tool for it high axial resolution. With B-scan, which is combined with A-scan of successive points, OCT

provides cross-sectional images of macular, nerve fiber layer and optic nerve with high resolution. Images from OCT are often used to detect macular holes, macular edemas and retinal pigment epithelial detachment. A more important application of OCT is to monitor change of retinal thickness because of diabetic retinopathy.

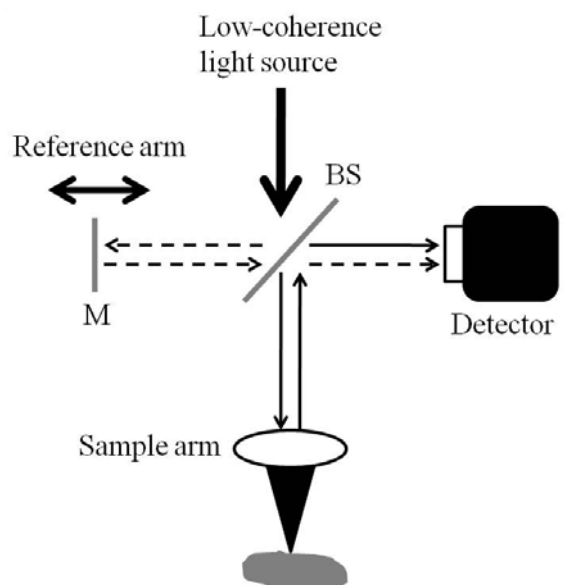


Fig. 2.5 Setup of OCT

An OCT combined with spectroscopic application was published in 2000[18,19]. It performs cross-sectional topographic images together with spectral information simultaneously. The bandwidth of OCT can be extended to more than 1000 nm in infrared[20]. The spectral resolution and the axial resolution of a OCT is correlated by a equation

$$\Delta z_{FWHM} \Delta K_{FWHM} \geq 4 \ln 2$$

It points out that OCT can not attains good axial and spectral resolution at the same time. For example, an OCT can achieve 100 μ m axial resolution with bandwidth of 10nm in infrared or 1 μ m axial resolution with 1000nm bandwidth in theory.

II.4 Discussion and Conclusion

In the last three sections, methods of retinal spectral imaging were introduced. Although fundus camera, spectroscopic OCT and cSLO all provide morphology of retina as well as spectral information, there are some differences between these techniques.

The lateral resolutions of the systems are all limited by the numerical aperture of eye and the ocular aberration. In fact, due to the ocular aberration, the lateral resolution is far from diffraction-limited case in every technique. The lateral resolution is usually around $5\mu\text{m}$ for human eye. Even with the confocal aperture, the improvement in lateral resolution is still not obvious as a result of the aberration.

The axial resolution of fundus camera and cSLO in human eye is around $300\mu\text{m}$ for a typical human eye[21]. In contrast, OCT separates signal from different depth for its interference-based detection, attaining axial resolution typically $10\mu\text{m}$ in human eye[22].

The frame rate of fundus camera can be several hundreds frame per second. As for spectral domain OCT[23], which is a technique modified from OCT, the acquisition rate achieves 20000A-scan/s. Thus spectral domain OCT can take around 500 cross-sectional images of retina per second. cSLO is limited by the scanning mechanism and is usually around video rate. They are all fast enough to overcome the saccade in principle, but there is dramatic difference between cSLO and the other ones.

Except fundus camera, both OCT and cSLO are able to perform optical-sectional images with same rate for transverse imaging, but the acquisition speeds of the two techniques to

acquire three-dimensional image stack have huge difference. Time taken by video-rate cSLO to acquire a three-dimensional stack composed of 300 512-by-512 images takes about 10 seconds or longer. Spectral domain OCT can take image stack of the same volume is acquired within 1 second.

It seems that spectral domain OCT can achieve retinal images of higher frame rate and axial resolution than SLO. However, A-scan based OCTs are not suitable to acquire cone cell mosaic because it takes too long to finish a transverse image. Only transverse scanning OCT can resolve cone cells[24]. A transverse scanning OCT is very similar to SLO except the coherence detection and thus the axial resolution, which is also around $10\mu\text{m}$.

As for the three different systems can all use mirror-based design, the bandwidths of them are limited to the light source and the retinal hazard region, which is from 400 nm to 1400nm. Arc lamps provide light from UV to infrared for fundus camera. Our cSLO contains a supercontinuum laser, for which the spectral band is from 475nm to $2\mu\text{m}$. Typical spectral OCTs have only limited bandwidth around 300~500nm in width[18,25] and there are also some OCT systems contain supercontinuum laser[26].

Fundus camera has a disadvantage, which is relatively high level of illumination intensity. In cSLO and OCT, illumination is taken point-by-point, thus reducing illumination intensity. Lower light level is important for keeping subject under stable and comfortable situation during examination.

Although the interference-based signal detection of OCT provides ideal axial resolution, there is also a drawback. In OCT images there are always speckles, which comes from the

interference between reference field and multiple-scattered field from sample[27]. Speckle noise downgrades contrast and makes it difficult to resolve boundary within images.

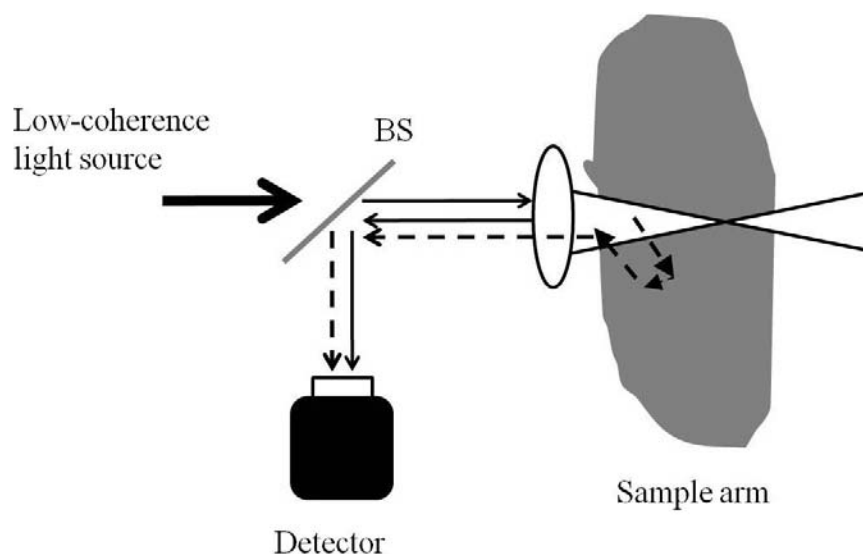


Fig. 2.6 Speckle formation in OCT. Dashed: multiple-scattered light

In summary, fundus camera, OCT and cSLO are used in different applications. Fundus camera has the simplest design and is thought to be the first step of ophthalmic examination. cSLO performs optical-sectional images and fast transverse scanning. Traditional OCT gives cross-sectional images with best axial resolution, but there is a dilemma between axial and spectral resolution because the axial resolution is coupled with spectral resolution. Transverse scanning OCT provides *en-face* images with axial resolution identical to traditional OCT. By adapting appropriate light source, all the systems above can acquire retinal spectral images. The choice between the techniques depends on the aim of the study. For measuring absorption spectrum of a single cone cell with spectral resolution around 10 nm, transverse scanning OCT gives the best axial resolution, but cSLO is an alternative with simpler design, which provides comparable performance except the axial resolution. As a result, we choose to develop a spectrally

resolved SLO, which can be upgraded to transverse scanning OCT if higher axial resolution is necessary.



Chapter III Experimental Setup

III.1 Overview

We have previously discussed the advantages of spectral retinal imaging. Contrast is enhanced by different spectral characteristics of subjects. However, most of the cSLO systems are monochromatic or have only several spectral lines[13,28,29]. The main reason is the lack of suitable broadband light sources and scanning systems.

Fig. 3.1 is the setup of our spectrally resolved cSLO. The system is composed of four main components, which are light source, scanning system, signal detection and frame grabbing. In the following sections, details of each component will be introduced. In the last section, specifications of the elements of the spectrally resolved cSLO are listed.

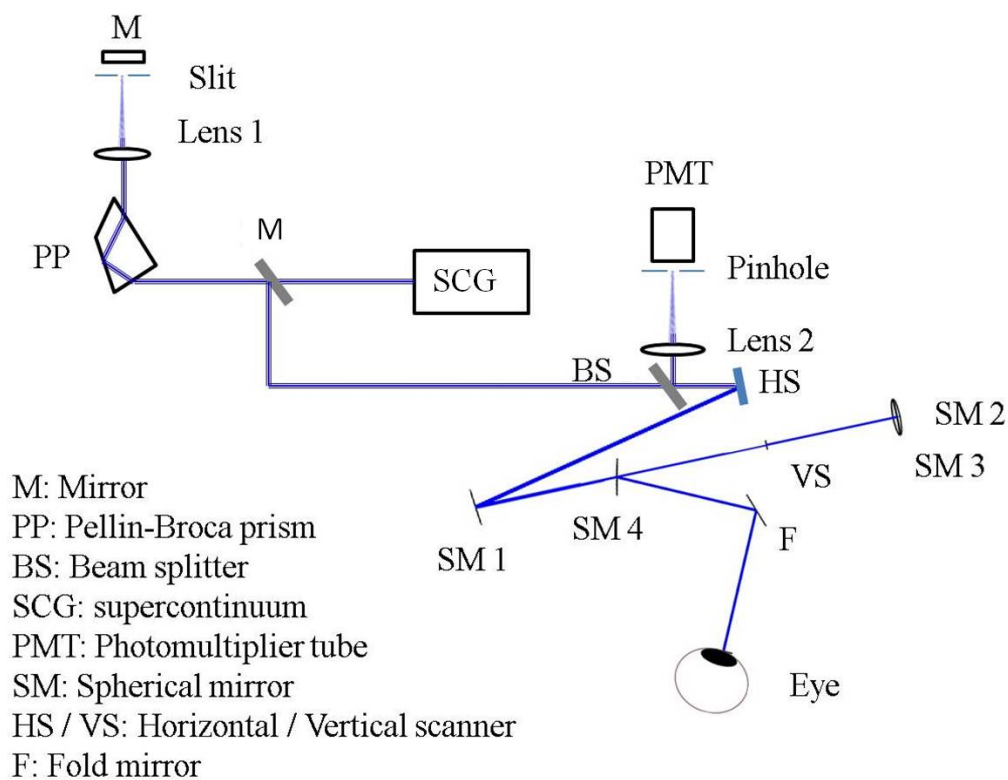


Fig. 3.1 Spectrally resolved cSLO

III.2 Light Source

In 1999, Reinholz et al published a multicolor cSLO[28], which simultaneously acquires retinal images of three different colors. The laser source is composed of a HeNe laser, a Ti-sapphire laser and an Ar-ion laser. Dichroic mirrors are introduced to combine three laser beams. The bandwidth of this system is adequate for performing true color images, but is far below the criterion of spectral imaging. Meanwhile, the collinearity of the three wavelengths is not easily maintained. Another spectral cSLO system chooses Ar/Kr laser[29], which provides nine different wavelengths from 476nm to 676nm. Even though there is significant improvement, it is still not enough for spectrum measurement in visible band.

To complement the insufficient spectrum of the previous lasers, supercontinuum is chosen as our laser source. Supercontinuum is generated by the combination of several nonlinear optical effects, which occurs when high-intensity laser pulses are pumped into a photonic crystal fiber (PCF). The bandwidth of the laser can be extended to several octaves in visible to near infrared region[30]. The spectrum of supercontinuum is continuous, providing high spectral resolution for multicolor imaging. The collinearity of supercontinuum is guaranteed because all of the wavelengths are from the same point source, which is the core of PCF.

A wavelength selector (Fig. 3.2) is constructed to select desired bands from the supercontinuum. The supercontinuum laser beam first passes through a Pellin-Broca prism, a grating or other dispersion media. After the prism, an achromatic lens is used to collimate the direction of different wavelengths. The lens also focuses light into a sequence of spots,

which are of different wavelengths. A slit at the focus is used to select the desired wavelength and a mirror reflects it back, passing through the lens and the prism again. The mirror slightly tilts downwards to isolate the reflected beam from the original path. The spectral resolution of the wavelength selector is around 10 nm in visible region.

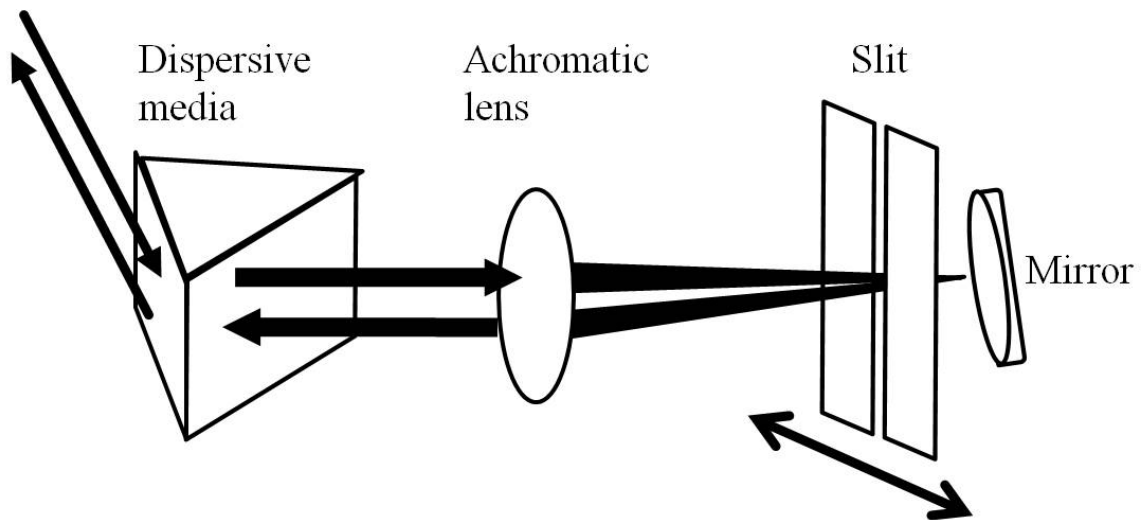


Fig. 3.2 Wavelength selector. The slit and the mirror are free to move along horizontally to select different wavelength.

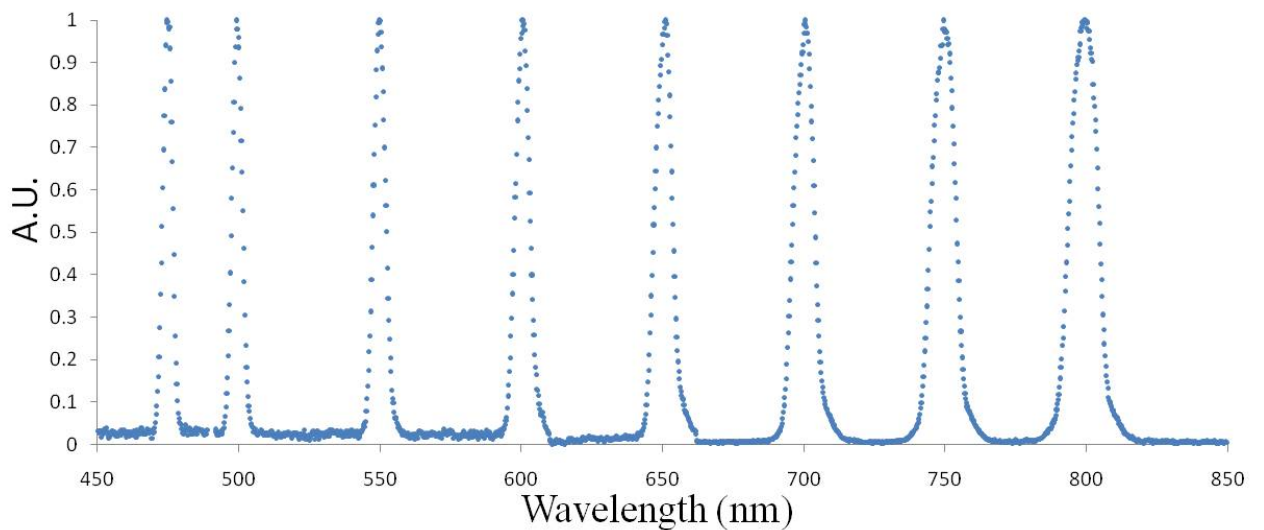


Fig. 3.3 Selected wavelengths from wavelength selector. Spectral resolution is around

10nm

III.3 Scanning System

Convex lenses are widely used for laser scanning system. However, the bandwidth of lens is usually only 400nm in visible region, which is restricted by antireflection coating. The wavelength-dependent refraction index also gives rise to achromatic aberration. To extend the bandwidth of scanning system, some use mirrors with metallic coating to replace lenses in telescopes. Reflectance of metallic coating is generally over 90% from visible to infrared, thus broadening bandwidth of scanning system and removing achromatic aberration at the same time. Nevertheless, things do not come out perfect. Concave mirrors introduce severe off-axis aberrations and downgrade the performance of cSLO system.

In normal mirror-based scanning system, beam makes successive reflection at mirrors' surfaces. Each reflection is in the same direction and thus accumulates aberrations, which include astigmatism, coma and other higher order terms. Astigmatism, which is the major term of off-axis aberration, results from the focal length difference between sagittal plane and tangential plane[31].

To compensate the astigmatism, a novel design of mirror-based scanning system is demonstrated by Yu et al.[32], the previous developer of this spectral cSLO system. In this scanning system, astigmatism is compensated by changing the plane of reflection at every other mirror. Coma is also compensated by combining two such telescopes, and they are just adequate for constructing a two-dimensional scanning system. With numerical simulation, proper reflection angle at every mirror is calculated. The result is confirmed by experience and diffraction-limited performance is achieved. Fig. 3.5 is the wavefront measurement of a beam passing through the scanning system. The root-mean-square (RMS)

wavefront error is 0.030 waves at 530nm. According to the Marechal criterion, diffraction limit is defined as a RMS wavefront error less than 1/14 wavelength. Thus our scanning system has diffraction-limited performance.

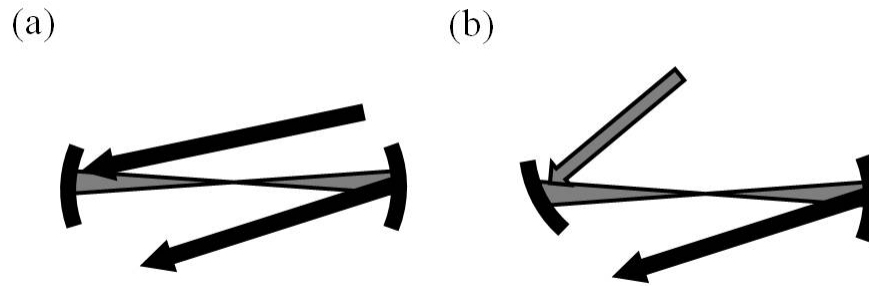
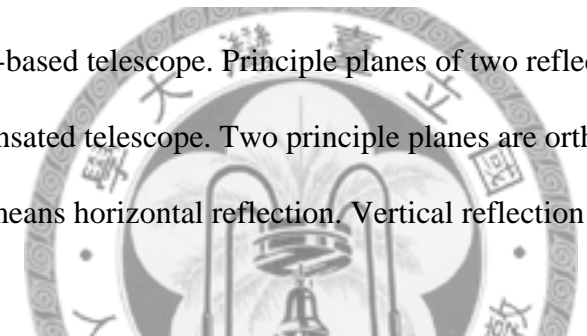


Fig. 3.4 (a) Mirror-based telescope. Principle planes of two reflections are the same. (b) Astigmatism-compensated telescope. Two principle planes are orthogonal. Change from gray to black means horizontal reflection. Vertical reflection is straight-gray.



Peak-to-valley = 0.150 waves
 RMS = 0.030 waves
 Wavelength = 0.530 mic
 Optical power = -0.018 D

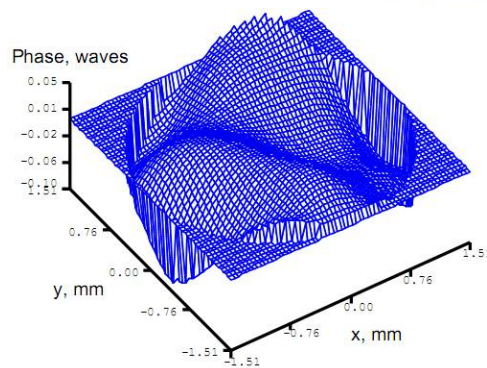


Fig. 3.5 Wavefront measurement of the scanning system.

A pair of scanning mirrors is adapted to the scanning system. They are a 16 kHz resonant scanning mirror and a galvo scanning mirror working in 28.5Hz. With this scanning

system we are able to acquire spectral images of retina 28.5frame/s.

III.4 Signal Detection and Frame Grabbing

After being scattered at the retina, signal is collected by the lens and goes backwards along the path of illumination. Since the path is fixed before entering the scanning system, signal from entire retina will be “descanned” and goes to the same destination. A beam splitter is placed before scanning system to separate signal from the illumination beam. Signal is then focused onto a pinhole, which is at the conjugate plane of retina to block out the out-of-focus light. A photomultiplier tube (PMT) is right after the pinhole, transducing light signal into current signal. The current signal from PMT is first transformed into voltage signal by an amplifier, and then received by a data acquisition device (DAQ), which is integrated with Labview.

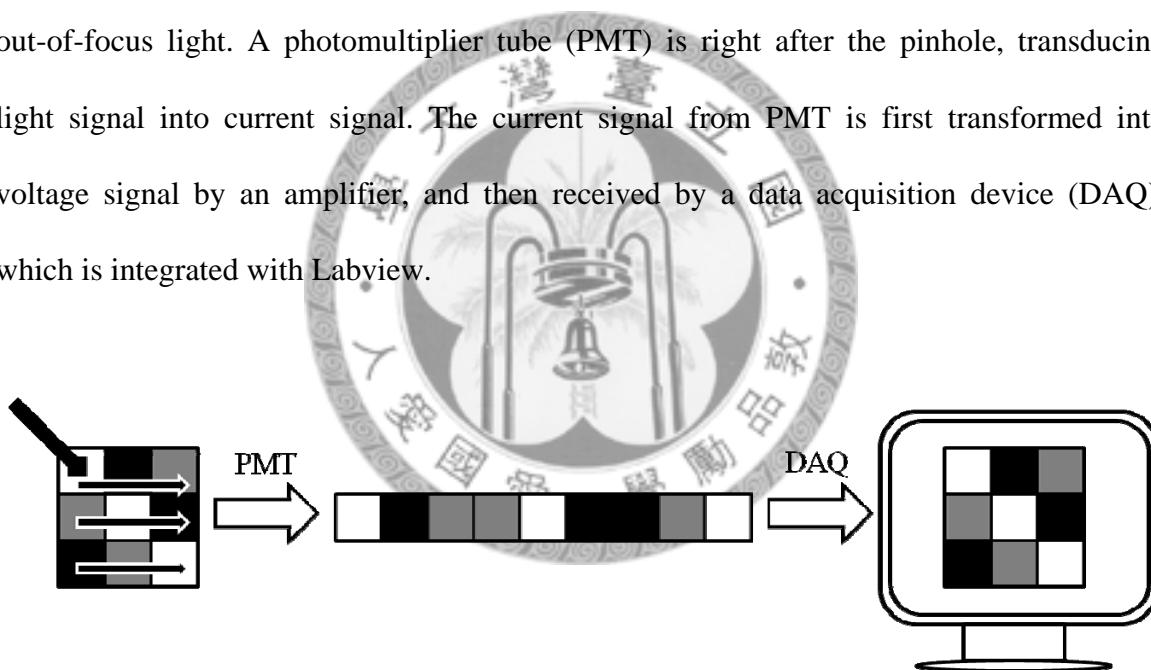


Fig. 3.6 Concept of frame grabbing with DAQ

The sampling rate of DAQ is up to 10MHz, which is the typical value in my application. The analog voltage signal from the PMT is sampled and turned into digital signal by DAQ. Data acquisition is synchronized with the scanning mirrors by the frame triggering signal from their driver. After receiving a frame triggering signal, the DAQ starts sampling data of a specific number and wait until the next triggering signal. The acquired one-dimensional data array is reshaped into two-dimensional array by software and

converted into an image.

IV.5 Specification of Devices

Laser source

	Model number/ <i>manufacturer</i>	Description	Notes
Supercontinuum laser	SC-400-2 <i>Fianium Ltd</i>	Pulse width: 5 ps. Repetition rate: 20 MHz. Wavelength range: 450 ~ 2000 nm	

Electronics and software programs

	Model number/ <i>manufacturer</i>	Description	Notes
Computer	—	CPU: Intel Core (R) i7 CPU 2.67 GHz. RAM: 3 GB.	
Data acquisition device	PCI-6115 <i>National Instrument</i>	12-Bit 10 MS/s/ch 4 analog inputs	
PMT amplifier	C6438-01/ <i>Hamamatsu Corp.</i>	Gain: 25 mV/ 1 μ A. Gain bandwidth: DC to 50 MHz. Max. output noise: 8 mV.	
Video acquisition program	Labview <i>National Instrument</i>		
Optical design program	ZEMAX-EE/ <i>ZEMAX Development Corp.</i>	—	

Scanners and the detector

Scanners	PLD-XYG/ <i>Electro-Optical Products Corp.</i>	The fast (resonant) and slow (galvo) Scanners are locked in raster scanning mode. Frequency: 16 KHz (fast)/ 28.5 Hz (slow)	HS, VS
PMT	R2949/ <i>Hamamatsu Corp.</i>	Spectral response: 185~900 nm Anode sensitivity: 410000 A/W Dark current: 2 nA	PMT

Opto-mechanics

	Model number/ <i>manufacturer</i>	Description			Notes
		Dimensions	Resolution	Tunable range	
Mount	U100-A3K/ <i>Newport Corp.</i>	1" aperture	3.8 arc sec	±7°	
	U100-A-LH-3K/ <i>Newport Corp.</i>	1" aperture	3.8 arc sec	±7°	
	KM100/ <i>Thorlabs Inc.</i>	1" aperture	—	±4°	
Stage	06PTS-0.5M/ <i>Unice E-O Service Inc.</i>	60×60×22 mm ³	10 μm	13 mm	For slit
	06DTS-3M/ <i>Unice E-O Service Inc.</i>	182×165×194 mm ³	5 μm	25 mm for each axis	For confocal pinhole
Pinhole	P50S/ <i>Thorlabs Inc.</i>	50-μm diameter	2-μm tolerance	—	P
Slit	NT40-488/ <i>Edmund Optics Inc.</i>	56×38×22 mm ³	10 μm	0~6.35 mm	Slit
Iris	ID25/ <i>Thorlabs Inc.</i>	43-mm diameter	—	1~25-mm aperture	

Optics

	Model number/ <i>manufacturer</i>	Description			Notes
		Radius of curvature	Surface coating/ spectral range	Surface accuracy	
Spherical mirror	SMCC-1037-0.40-C/ <i>CVI Technical Optics Ltd.</i>	400 mm	EAV/ >90% reflectance within 400~10000 nm	$\lambda/10$	
	10DC200/ <i>Newport Corp.</i>	200 mm	AL.2/ >85% reflectance within 400~6000 nm	$\lambda/4$	
Beam splitter	BS013/ <i>Thorlabs Inc.</i>	—	—	$\lambda/10$	

Table 3.1 Part lists. λ here is 633 nm.



Chapter IV Results and Discussion

IV.1 Spectral Images of Artificial Eye

To testify the spectral imaging ability of the spectrally resolved cSLO, spectral images of artificial eye are first demonstrated. The artificial eye is composed of a lens and a CCD. This is the simplified model of real eye, in which the CCD is regarded as retina. On the CCD there are three types of bandpass filters with different spectral windows. We capture spectral images of the CCD (Fig. 4.1) with an objective (Olympus, 40X, $f = 1.6$ mm).

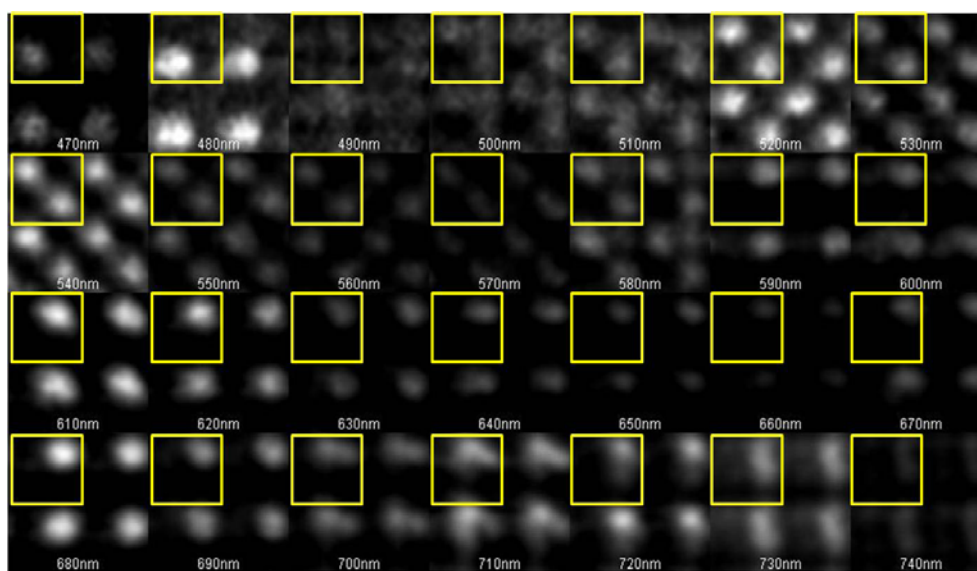


Fig. 4.1 CCD spectral images taken with objective. Each side of the square is $7.5\mu\text{m}$.

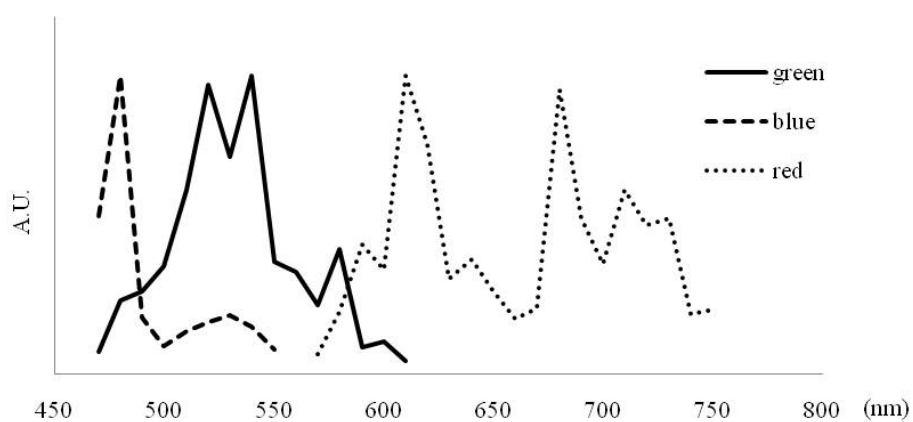


Fig. 4.2 Measured transmissions of filters on CCD

Resolution is defined by the distance that intensity drops to half maximum at an edge of a CCD pixel (Fig. 4.3). Resolution with 670 nm is 1.41 μm and the measured diameter of a filter is 4.1 μm . The corresponding theoretical resolution is 1.37 μm .

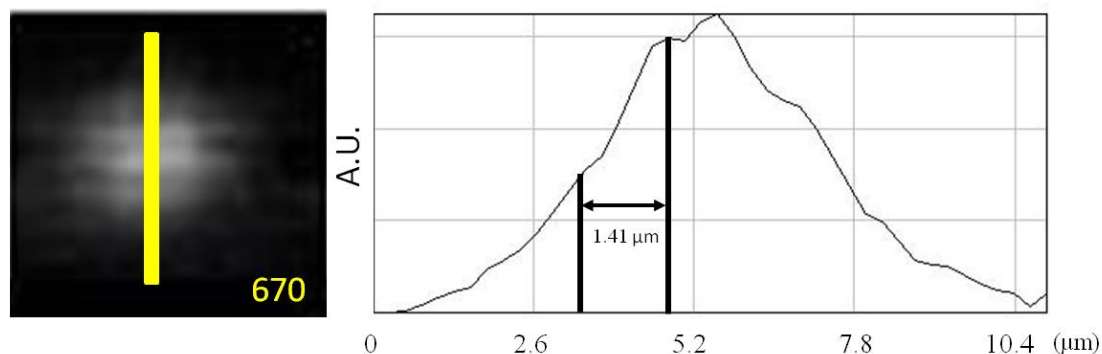


Fig. 4.3 Resolution analysis of Fig. 4.1.

In fig. 4.1 I use the squares to identify the same filter cell in every wavelength. We can see different density for each type of filter. The arrangement is called Bayer filter mosaic. We suppose the signal comes from the CCD's surface. Thus if light didn't pass a filter, it would be no signal there. It means that the signal is proportional to the transmission of filters. In fig. 4.1 there are two equally bright pixels from 520 nm to 570 nm, which are thought as the pixels under the green filters. The pixel at lower left is a blue pixel for the signal at 470 nm and 480 nm. The other one is a red pixel. By measuring the intensity at the filter, corresponding spectrum is obtained (Fig. 4.2).

Images are also acquired with lens from artificial eye itself (fig. 4.5). Bayer filter mosaic is also found. The CCD pixels shift toward the same direction when illumination wavelength is changed. This is because of the off-axis incident of lens and the different effective focal lengths between wavelengths (fig. 4.4). The images are manually registered to compensate the shift. In this picture we can see the spectrums of the pixels are different from fig. 4.1.

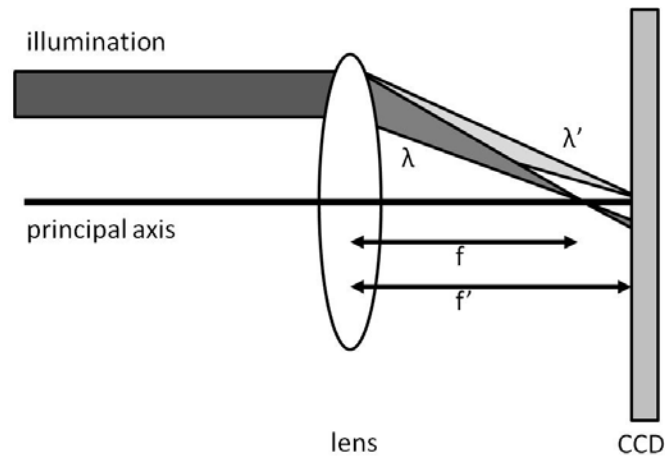


Fig. 4.4 Image shift due to wavelength switching.

There are some difference between fig. 4.1 and fig. 4.5. First, there are multiple pixels per cell from 470 nm to 490 nm in fig. 4.5, but there is only one pixel per cell in the corresponding wavelengths of fig. 4.1. Second, there are two pixels in images from 500 nm 540 nm, but the signal intensity of them is different. As for fig. 4.1, there are also two pixels but with equal brightness. Third, there is only one pixel per cell in both images with 610 nm or longer wavelength. This suggests the contrast in fig. 4.5 is different from fig. 4.1 for 540 nm and shorter wavelengths.

There are two equally bright pixels at the upper left and the lower right of a filter cell in 470 nm, 480 nm and 490 nm. Since the density of them is twice of the other two pixels, they should be green filters. The other two pixels appear different intensity in fig. 4.5 from 500 nm 540 nm, so they should be different types of pixels. These images tell us the contrast is opposite to fig. 4.1. This is because that when fig. 4.5 is imaging with 540 nm and shorter wavelengths, the signal is from the surface of filters. Light reflected from the filters is negative related to the transmission of the filters and this is the reason of the

opposite contrast.

However, there is only one pixel in each filter cell after 610 nm in both fig. 4.1 and fig. 4.5. Since both green and blue filter have zero transmission after 610 nm, we should not be able to observe these filters without any of them. It tells us that it is red pixel in 610 nm image. So this time the signal source is moved to the surface of CCD and the contrast comes back to the case of fig. 4.1. This suggests that there is longitudinal chromatic aberration for the lens. When illumination wavelength is changed, the sectioning depth may be changed by the longitudinal aberration. In contrast, there is no such aberration in fig. 4.1 because the aberration is corrected in objective.

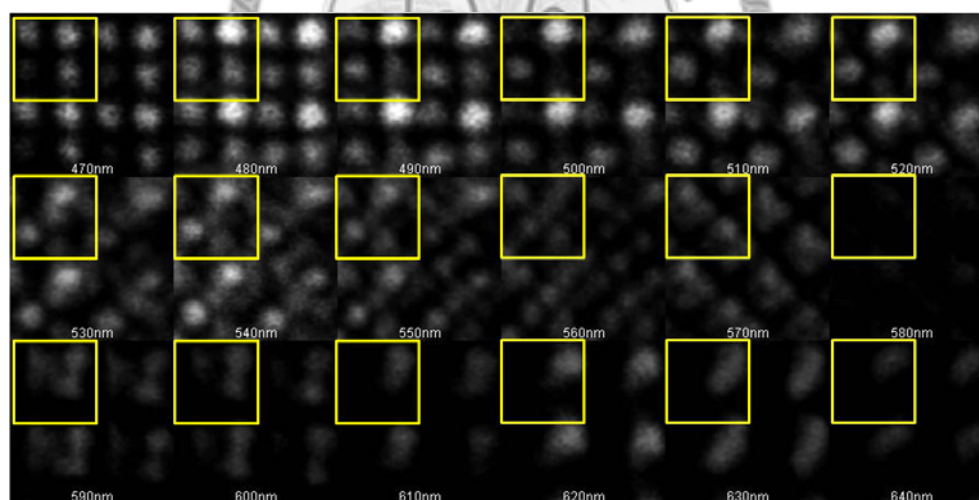


Fig. 4.5 CCD spectral images taken with lens from artificial eye

IV.2 Retinal Spectral Images of Zebrafish

To demonstrate the ability of performing retinal spectral images *in-vivo*, zebrafish is an ideal subject because it is model animal of many vertebrate researches. There are many advantages for the use of zebrafish. For example, zebrafish is easily maintained and its

development is rapid. This is helpful for reducing the cost of experiments. Meanwhile, zebrafish's retina is like human retina but is rather simpler than other vertebrate species. The well established genetic methods and relative simplicity of retina makes zebrafish important to understand human disease and central nervous system.

Using zebrafish can also ignore the irregular shape of cornea, which is one of the main reasons of ocular aberration of human eye. The refractive index of the lens increases with radius from 1.36 to 1.54[33]. The cornea is optically ineffective under water. It is because the refractive index of water (1.34) is nearly identical to aqueous fluid and cornea[34]. But when the eye is exposed to air, refraction at the cornea changes the direction of incident light and causes myopia. To make sure that the laser focuses on the retina, zebrafish is kept underwater during experiment.

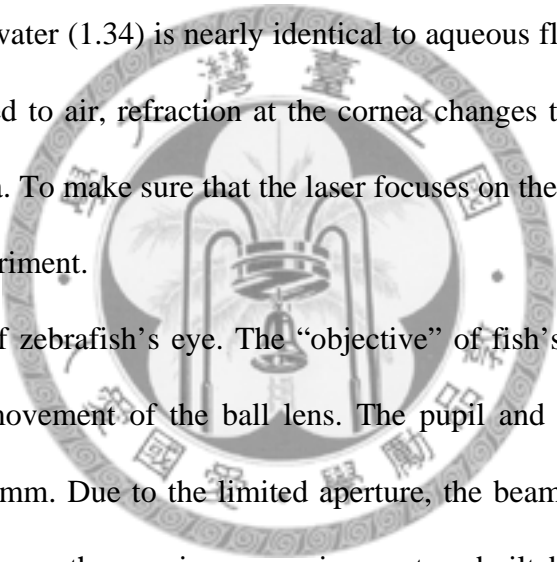


Fig. 4.6 is a diagram of zebrafish's eye. The "objective" of fish's eye is a ball lens, and focusing depends on movement of the ball lens. The pupil and lens diameters of adult zebrafish are around 1 mm. Due to the limited aperture, the beam size must be around 1 mm in diameter. However, the previous scanning system built by Yu et al. includes a telescope composed of spherical mirrors, which are 20 cm and 40 cm in radius respectively. This pair of mirrors expands the beam twice in diameter, excluding much of the laser from illuminating the retina. To prevent the overfilling of aperture, I change the design of the scanning system. The focal length of mirrors in the previous version of scanning system is 10, 10, 10 and 20 cm. The order is a change into 20, 10, 10, 10 cm to makes further contraction.

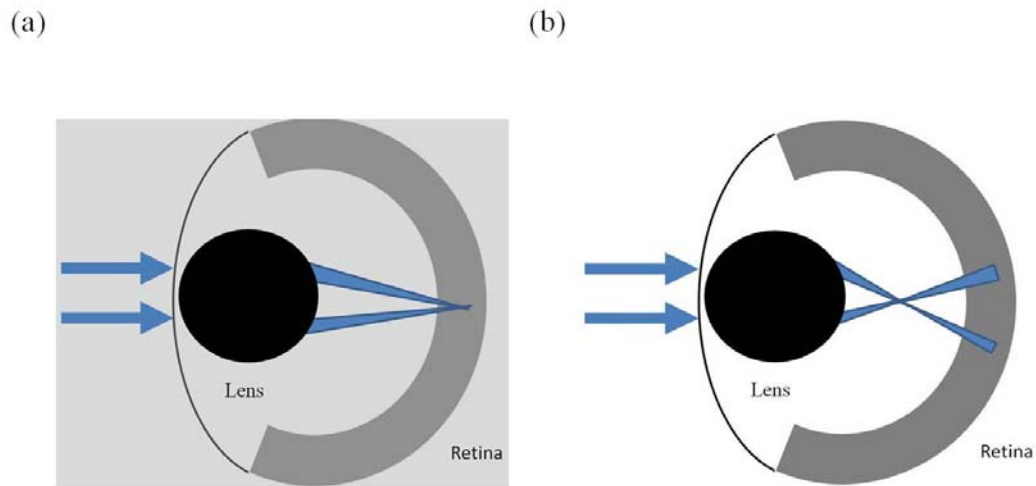


Fig. 4.6 Light in fish's eye, which is (a) under water and (b) in air.

The experiment requires illumination of visible light at the retina. It generates visual response and thus making the fish unstable during experiment. As a result, we put the zebrafish into water at 0°C for 5 minutes to achieve anesthesia.

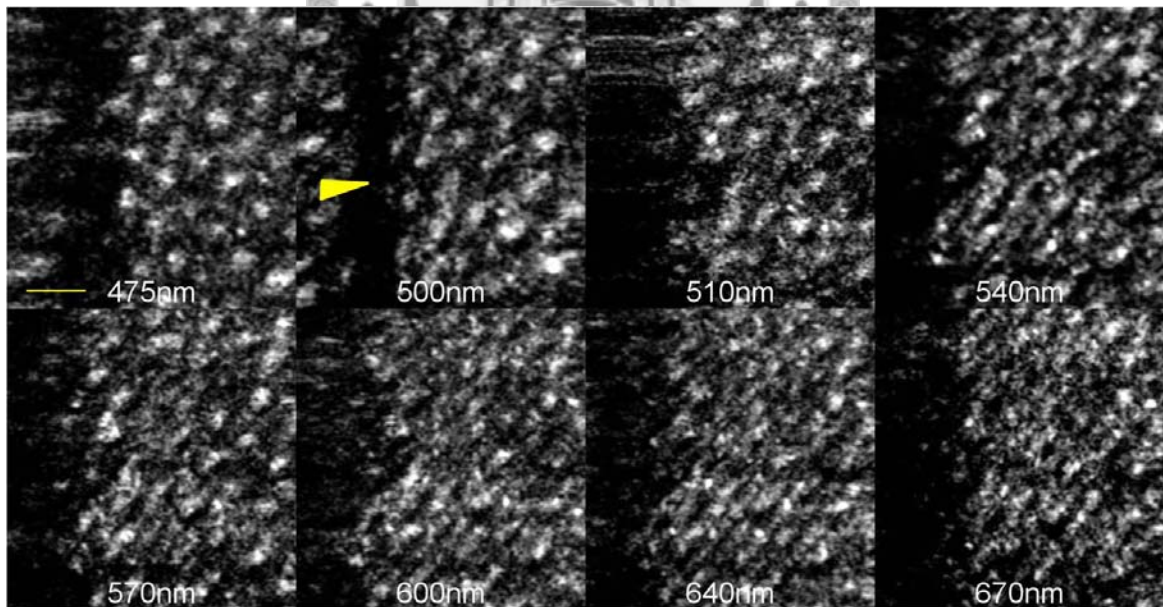


Fig. 4.7 Retinal spectral images of zebrafish. The scale bar is 10 μm .

Fig. 4.7 is the retinal spectral image set acquired with the supercontinuum laser. These images are optical sections of photoreceptor layer. Blood vessel, as indicated by the arrow

in 500 nm image, and cone cells are observable. The blood vessel is dark because scattering happens mainly at its surface and scattered light is blocked by the confocal pinhole. Images are manually registered with the cone distribution.

The image width w is calculated by

$$w = \theta \times f$$

, where θ is the scanning angle and f is the effective focal length. The scanning angle is 3.8° by 5.3° . The effective focal length of lens is $700 \mu\text{m}$, which is simulated with Zemax according to the parameter from previous studies[33]. The size of the original image is $46 \mu\text{m}$ by $65 \mu\text{m}$. Images in fig. 4.7 are $32 \mu\text{m}$ by $40 \mu\text{m}$, which are cropped from the original images. The power of laser is $120 \mu\text{w}$ after the scanning system. The intensity is around 10^{10} photons / μm^2 *s. Frame rate is 28.5 frames per second.

To calculate the resolution, we first assume the absorbance of every single cone cell is homogeneous laterally. That is, cone cells are thought as color filters with sharp edge and specific spectrums. With this assumption we can find the 510 nm lateral resolution to be $3 \mu\text{m}$ with the same method in the previous CCD case. With pupil diameter 1 mm, effective focal length $700 \mu\text{m}$ and wavelength 510 nm, the theoretical lateral resolution is 400 nm. The experimental result is much worse than theory. It is because of the aberration of the ball lens. To find the axial resolution, we use the experimental $3 \mu\text{m}$ lateral resolution to find the effective NA, which is 0.1. By inserting this into the axial resolution equation, we find the axial resolution is $80 \mu\text{m}$.

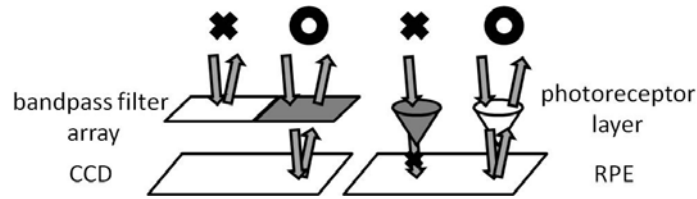


Fig. 4.8 Comparison of filters between artificial eye and real eye.

Photoreceptors basically absorb light, and the signal in SLO is light reflected by retinal pigment epithelium [6]. Absorbances of different subtypes are separated in wavelength and the photoreceptors are like absorptive optical filter. For example, since the green cone absorbs blue light[35], there would be no signal for green cones in a blue SLO images, as indicated in fig. 4.8. Thus the absorbance is negatively correlated to the signal intensity. On the other hand, the green bandpass filter on CCD allows green light pass through but wavelength outside the transmission window and only light reflected at the CCD can pass through the confocal pinhole.

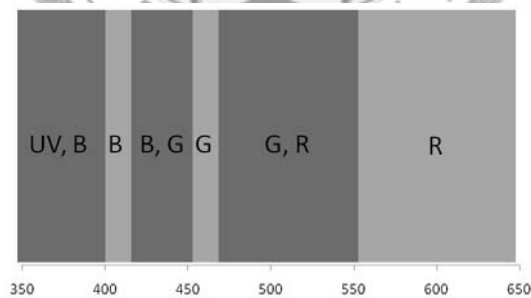


Fig. 4.9 Absorption bands of photoreceptors. UV: short single B: long single G: green cone R: red cone

I would like to compare the effect of longitudinal chromatic aberration of artificial eye and zebrafish. As mentioned in the last section, the longitudinal chromatic aberration of lens may change the sectioning depth. This effect is not crucial for zebrafish. The depth

difference between double cones and short cones is around $50\ \mu\text{m}$ [36]. However, the axial resolution is $80\ \mu\text{m}$ and the Zemax simulation of the ocular lens gives the effective focal length difference between 700nm and $450\ \text{nm}$, which is only $10\ \mu\text{m}$. There is also research point out that the longitudinal chromatic aberration in fish lens causes 5% change in effective focal length from $436\ \text{nm}$ to $630\ \text{nm}$ [37], which is around $35\ \mu\text{m}$. These are evidences for the reasonableness that we can always see cone cells when switching the illumination wavelength.

There are four subtypes of cone photoreceptors in a zebrafish, which are red, green, long single and short single cone. Red and green cones are bound together and called double cone. On retina, the cones are in a precise two-dimensional pattern. Double cones are aligned in a row, while short and long single cones are aligned alternatively[38]. Short singles and long singles have similar absorbance above $475\ \text{nm}$ [35]. According to the discussion in the last paragraph, the cone cells in $475\ \text{nm}$ image should be single cone cells. Since we have only images from $475\ \text{nm}$ to $720\ \text{nm}$, it is impossible to distinguish the two single cones in this spectral range. The nearest neighbor distances of short and long singles are longer than $10\ \mu\text{m}$ [38]. In the $475\ \text{nm}$ image, I use a $10\ \mu\text{m}$ bar to indicate the nearest neighbor distance. There is apparently another cone cell within the nearest neighbor distance. This is an evidence of co-existence of the two single cone subtypes.

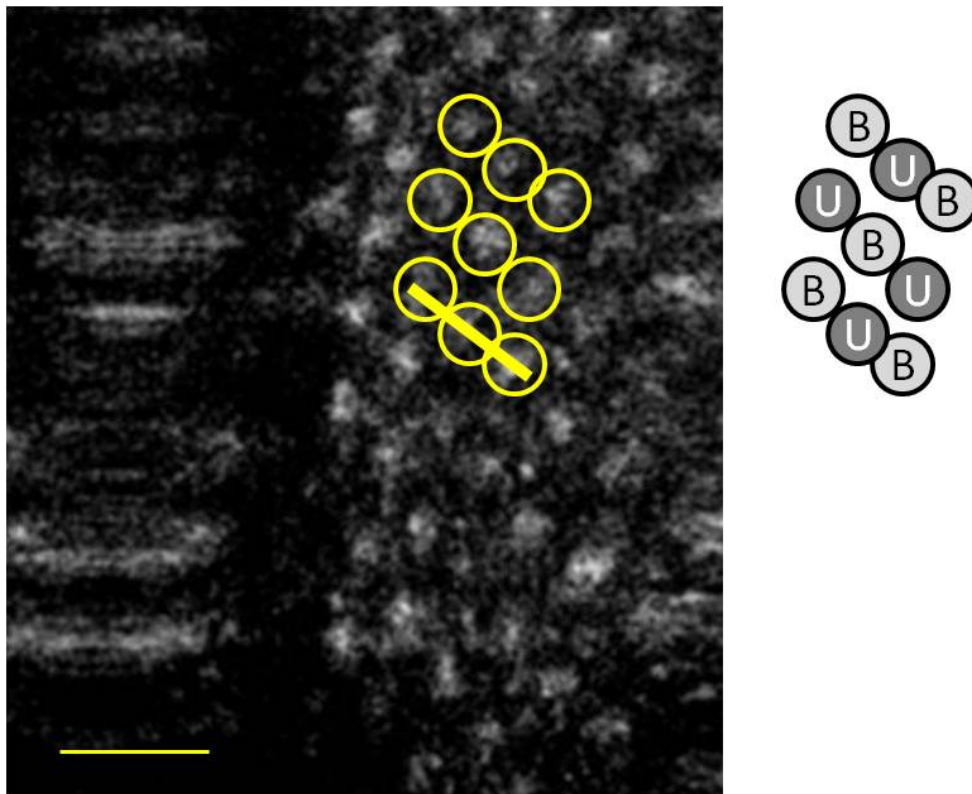


Fig. 4.10 Mosaic of short and long single cone. B: long single cone. U: short single cone.

Scale bar: 10 μm .

To further find out the possible locations of green and red cones, we made some image processing. In fig. 4.11, (a) is the image of 570nm image subtracts 475 nm image. Since the absorption band edge of the green cones fall at 550 nm, the difference between 570 nm image and 540 nm image should give us the possible location of green cones. (b) in fig. 4.11 is obtained by subtracts 570 nm image with 670 nm image. This time the resulting image gives us the location of reds cones. We add these two images and we have (c), which is the image of double cones. The vacancies in (c) also give us the locations of long and short single cones.

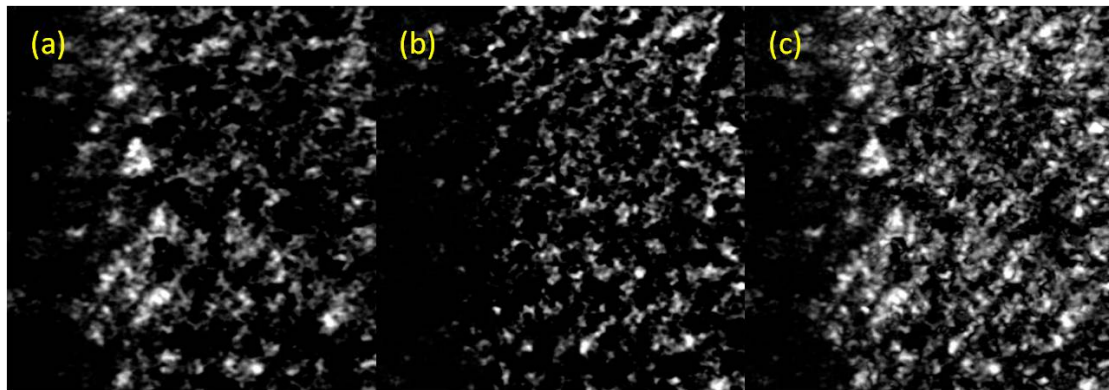


Fig. 4.11 Processed images. (a) 570nm image subtracts 475 nm image. (b) 670 nm image subtracts 570 nm image. (c) Overlap of (a) and(b)

There are some problems in this system. First, wavelength modulation is done by a manual translation stage. It usually takes seconds to switch between wavelengths. Movement of zebrafish due to breathing or struggle changes the field of view during wavelength switching. This makes trouble to spectrum analysis because we are not able to calculate spectrum at the same target area thus introducing statistical error.

One way to overcome this problem is to replace the prism with an acousto-optic modulator (AOM). With an AOM, whose rise time is only several nanoseconds, we are able to switch the illumination wavelength between every frame by program. Although it is convenient to switch wavelength with an AOM, the working bandwidth of AOM is usually under 400 nm and limits the bandwidth of system. The other solution is introducing automatic translation stage. By controlling the frame grabbing and wavelength switching with the same program, time to acquire spectral images will be greatly reduced. No matter introducing AOM or automatic translation stage, we can further register the characteristics in the field of view and match the spectral images by program.

The other problem is the distortion of the image. As introduced in the previous cSLO section, resonant scanners rotate sinusoidally. It stays at the edge longer and at the center shorter. The constant rate signal sampling would collect more pixels from the edge of field of view and less from the center. To restore the scale of the image, we can develop a program to recover the real relative displacement between the pixels according to the sinusoidal motion of the scanner. Another way is to use sinusoidal pixel clock. This way, the displacement between every other pixel is equalized and the image will be free from distortion.



IV.3 Conclusion

Retinal spectral imaging provides spectral information of fundus with microscopic scale. In this thesis, we have demonstrated a spectrally resolved cSLO. To overcome the two main problems in previous retinal spectral imaging systems, which are limited bandwidth and off-axis aberration, we introduce supercontinuum and novel design of mirror-based scanning system. Supercontinuum is chosen as the broadband light source. The continuous spectrum of supercontinuum provides wavelength from visible to infrared spectral imaging. To overcome the limited spectrum of lenses in traditional scanning system, we use concave mirrors instead. For the off-axis aberration of concave mirror, a mirror-based scanning system with stereo-positioning design is introduced, which compensate the astigmatism and coma is usual mirror-based scanning system without any other elements.

With the spectrally resolved cSLO, we are able to analyze the spectrum of fundus in artificial eye with the spectral images. Diffraction-limited performance is achieved with both the objective and lens of artificial eye. We also acquire retinal spectral images in zebrafish. Pattern of photoreceptor mosaic and blood flow are observed. By switching the illumination wavelength, single cone cell is resolved without any complicated aberration correction. This system can be used to trace retinopathies such as age-related macular degeneration, glaucoma, diabetic retinopathy. Microcirculation can also be monitored noninvasively with spectrally resolved cSLO. This retinal imaging system is adequate for ophthalmic researched and biomedical studies, providing unlimited possibilities.

Figure Index

Fig. 2.1	Setup of a fundus camera.	15
Fig. 2.2	Concept of confocal microscope.	19
Fig. 2.3	The scheme of a cSLO.	22
Fig. 2.4	Telescope for moving beam scan.	23
Fig. 2.5	Setup of OCT.	26
Fig. 2.6	Speckle formation in OCT. Dashed: multiple-scattered light.	29
Fig. 3.1	Spectrally resolved cSLO.	31
Fig. 3.2	Wavelength selector.	33
Fig. 3.3	Selected wavelengths from wavelength selector.	33
Fig. 3.4	Mirror-based telescope.	35
Fig. 3.5	Wavefront measurement of the scanning system.	35
Fig. 3.6	Concept of frame garbbing with DAQ.	36
Fig. 4.1	CCD spectral images taken with objective.	40
Fig. 4.2	Measured transmissions of filters on CCD.	40
Fig. 4.3	Resolution analysis of Fig. 4.1.	41
Fig. 4.4	Image shift due to wavelength switching	42
Fig. 4.5	CCD spectral images taken with lens from artificial eye	43
Fig. 4.6	.Light in fish's eye, which is (a) under water and (b) in air.	45
Fig. 4.7	Montage of retinal spectral images of zebrafish. The scale bar is 10 μm .	45
Fig. 4.8	Comparison of filters between artificial eye and real eye.	47
Fig. 4.9	Absorption bands of photoreceptors.	47
Fig. 4.10	Mosaic of short and long single cone.	49

Fig. 4.11 Processed images.

50

Table Index

Table 3.1 Part lists.

37



Reference

- 1 Wollstein, G., Garway-Heath, D. F. & Hitchings, R. A. Identification of early glaucoma cases with the scanning laser ophthalmoscope. *Ophthalmology* **105**, 1557-1563 (1998).
- 2 Fong, D. S., Aiello, L. P., Ferris, F. L. & Klein, R. Diabetic retinopathy. *Diabetes Care* **27**, 2540-2553 (2004).
- 3 Smith, R. T., Chan, J. K., Busuoiu, M., Sivagnanavel, V., Bird, A. C. & Chong, N. V. Autofluorescence characteristics of early, atrophic, and high-risk fellow eyes in age-related macular degeneration. *Invest. Ophthalm. Vis. Sci.* **47**, 5495-5504 (2006).
- 4 Hiroshiba, N., Ogura, Y., Sasai, K., Nishiwaki, H., Miyamoto, K., Hamada, M., Tsujikawa, A. & Honda, Y. Radiation-induced leukocyte entrapment in the rat retinal microcirculation. *Invest. Ophthalm. Vis. Sci.* **40**, 1217-1222 (1999).
- 5 Katsumi, O., Timberlake, G. T., Hirose, T., Velde, F. J. & Sakaue, H. Recording pattern reversal visual evoked response with the scanning laser ophthalmoscope. *Acta Ophthalmol.* **67**, 243-248 (1989).
- 6 Berendschot, T., DeLint, P. J. & van Norren, D. Fundus reflectance - historical and present ideas. *Prog. Retin. Eye Res.* **22**, 171-200 (2003).
- 7 Schweitzer, D., Guenther, S., Scibor, M. & Hammer, M. Spectrometric investigations in ocular hypertension and early stages of primary open angle glaucoma and of low tension glaucoma — multisubstance analysis. *Int. Ophthalmol.* **16**, 251-257 (1992).
- 8 Schweitzer, D., Schrödel, C., Jütte, A., Blaschke, F., Königsdörffer, E. & Vilser, W. Reflectance spectrophotometry in the human ocular fundus. *Graef. Arch. Clin. Exp.* **223**, 207-210 (1985).
- 9 Berendschot, T., DeLint, P. & van Norren, D. Origin of tapetal-like reflexes in carriers of x-linked retinitis pigmentosa. *Invest. Ophthalm. Vis. Sci.* **37**, 2716-2723 (1996).
- 10 Beach, J., Ning, J. & Khoobehi, B. Oxygen saturation in optic nerve head structures by hyperspectral image analysis. *Curr. Eye Res.* **32**, 161-170 (2007).

- 11 Field, G. D., Greschner, M., Gauthier, J. L., Rangel, C., Shlens, J., Sher, A., Marshak, D. W., Litke, A. M. & Chichilnisky, E. J. High-sensitivity rod photoreceptor input to the blue-yellow color opponent pathway in macaque retina. *Nat. Neurosci.* **12**, 1159-1164 (2009).
- 12 Luo, G., Vargas-Martin, F. & Peli, E. The role of peripheral vision in saccade planning: Learning from people with tunnel vision. *J. Vision* **8**, - (2008).
- 13 Webb, R. H., Hughes, G. W. & Delori, F. C. Confocal scanning laser ophthalmoscope. *Applied optics* **26**, 1492-1499 (1987).
- 14 Laurent, M., Johannin, G., Leguyader, H. & Fleury, A. Confocal scanning optical microscopy and 3-dimensional imaging. *Biol. Cell* **76**, 113-124 (1992).
- 15 Webb, R. H. Confocal optical microscopy. *Rep. Prog. Phys.* **59**, 427-471 (1996).
- 16 Huang, D., Swanson, E. A., Lin, C. P., Schuman, J. S., Stinson, W. G., Chang, W., Hee, M. R., Flotte, T., Gregory, K., Puliafito, C. A. & Fujimoto, J. G. Optical coherence tomography. *Science* **254**, 1178-1181 (1991).
- 17 Povazay, B., Bizheva, K., Unterhuber, A., Hermann, B., Sattmann, H., Fercher, A. F., Drexler, W., Apolonski, A., Wadsworth, W. J., Knight, J. C., Russell, P. S. J., Vetterlein, M. & Scherzer, E. Submicrometer axial resolution optical coherence tomography. *Opt. Lett.* **27**, 1800-1802 (2002).
- 18 Morgner, U., Drexler, W., Kartner, F. X., Li, X. D., Pitris, C., Ippen, E. P. & Fujimoto, J. G. Spectroscopic optical coherence tomography. *Opt. Lett.* **25**, 111-113 (2000).
- 19 Leitgeb, R., Wojtkowski, M., Kowalczyk, A., Hitzenberger, C. K., Sticker, M. & Fercher, A. F. Spectral measurement of absorption by spectroscopic frequency-domain optical coherence tomography. *Opt. Lett.* **25**, 820-822 (2000).
- 20 Stumpf, M. C., Zeller, S. C., Schlatter, A., Okuno, T., Sudmeyer, T. & Keller, U. Compact Er : Yb : Glass-laser-based supercontinuum source for high-resolution optical coherence tomography. *Opt. Express* **16**, 10572-10579 (2008).

- 21 Donnelly Iii, W. J. & Roorda, A. Optimal pupil size in the human eye for axial resolution. *J. Opt. Soc. Am. A* **20**, 2010-2015 (2003).
- 22 Sakata, L. M., DeLeon-Ortega, J., Sakata, V. & Girkin, C. A. Optical coherence tomography of the retina and optic nerve - a review. *Clin. Exp. Ophthalmol.* **37**, 90-99 (2009).
- 23 Cense, B., Nassif, N. A., Chen, T., Pierce, M., Yun, S. H., Park, B. H., Bouma, B. E., Tearney, G. J. & de Boer, J. F. Ultrahigh-resolution high-speed retinal imaging using spectral-domain optical coherence tomography. *Opt. Express* **12**, 2435-2447 (2004).
- 24 Pircher, M., Baumann, B., Götzinger, E. & Hitzenberger, C. K. Retinal cone mosaic imaged with transverse scanning optical coherence tomography. *Opt. Lett.* **31**, 1821-1823 (2006).
- 25 Yi, J., Gong, J. & Li, X. Analyzing absorption and scattering spectra of micro-scale structures with spectroscopic optical coherence tomography. *Opt. Express* **17**, 13157-13167 (2009).
- 26 Stumpf, M. C., Zeller, S. C., Schlatter, A., Okuno, T., Südmeyer, T. & Keller, U. Compact er:Yb:Glass-laser-based supercontinuum source for high-resolution optical coherence tomography. *Opt. Express* **16**, 10572-10579 (2008).
- 27 Schmitt, J. M., Xiang, S. H. & Yung, K. M. Speckle in optical coherence tomography. *J. Biomed. Opt.* **4**, 95-105 (1999).
- 28 Reinholz, F., Ashman, R. A. & Eikelboom, R. H. Simultaneous three wavelength imaging with a scanning laser ophthalmoscope. *Cytometry* **37**, 165-170 (1999).
- 29 Gray, D. C., Merigan, W., Wolfing, J. I., Gee, B. P., Porter, J., Dubra, A., Twietmeyer, T. H., Ahamd, K., Tumber, R., Reinholz, F. & Williams, D. R. In vivo fluorescence imaging of primate retinal ganglion cells and retinal pigment epithelial cells. *Opt. Express* **14**, 7144-7158 (2006).
- 30 Stone, J. M. & Knight, J. C. Visibly ?White? Light generation in uniform photonic crystal fiber using a microchip laser. *Opt. Express* **16**, 2670-2675 (2008).
- 31 Hanna, D. C. Astigmatic gaussian beams produced by axially asymmetric laser cavities. *IEEE J. Quantum Elect.* **Qe 5**, 483-&

- (1969).
- 32 Yu, J.-Y., Liao, C.-S., Zhuo, Z.-Y., Huang, C.-H., Chui, H.-C. & Chu, S.-W. A diffraction-limited scanning system providing broad spectral range for laser scanning microscopy. *Rev. Sci. Instrum.* **80**, 113704-113705 (2009).
 - 33 Verma, Y., Rao, K. D., Suresh, M. K., Patel, H. S. & Gupta, P. K. Measurement of gradient refractive index profile of crystalline lens of fisheye in vivo using optical coherence tomography. *Appl. Phys. B-Lasers Opt.* **87**, 607-610 (2007).
 - 34 Greiling, T. M. S. & Clark, J. I. The transparent lens and cornea in the mouse and zebra fish eye. *Semin. Cell Dev. Biol.* **19**, 94-99 (2008).
 - 35 Cameron, D. A. Mapping absorbance spectra, cone fractions, and neuronal mechanisms to photopic spectral sensitivity in the zebrafish. *Visual Neurosci.* **19**, 365-372 (2002).
 - 36 Takechi, M., Hamaoka, T. & Kawamura, S. Fluorescence visualization of ultraviolet-sensitive cone photoreceptor development in living zebrafish. *Febs. Lett.* **553**, 90-94 (2003).
 - 37 Jagger, W. S. The optics of the spherical fish lens. *Vision Res.* **32**, 1271-1284 (1992).
 - 38 Raymond, P. A. & Barthel, L. K. A moving wave patterns the cone photoreceptor mosaic array in the zebrafish retina. *Int. J. Dev. Biol.* **48**, 935-945 (2004).